PERGAMON

International Journal of Heat and Mass Transfer 41 (1998) 3793–3805

International Journal of HEAT and MASS TRANSFER

Turbulent mixed convective heat transfer in the entrance region of a curved pipe with uniform wall-temperature

L. J. Li, C. X. Lin, M. A. Ebadian*

Hemispheric Center for Environmental Technology, Florida International University, Miami, FL 33199, U.S.A.

Received 10 October 1997; in final form 28 February 1998

Abstract

A fully elliptic numerical study was performed to investigate the buoyancy-affected, three-dimensional turbulent flow and heat transfer in the entrance region of a curved pipe. The renormalization group (RNG) k–ε model was used to simulate the turbulent flow and heat transfer in the pipe. A dimensionless ratio parameter, $\sqrt{Gr}/D_n\sqrt{1+Pr}$, was employed to characterize the relative magnitude of buoyancy and centrifugal effect on the secondary flow in the curved pipe. The computed results for forced convective flow and heat transfer show agreement with previous experimental data. It was found that the distribution of axial velocity and temperature rotated clockwise to a different extent depending on the ratio of $\sqrt{Gr}/D_n\sqrt{1+Pr}$. At higher Grashof numbers, the developing secondary flow field showed the existence of three vortices. The peripherally averaged Nusselt number and friction factor exhibit oscillatory behavior along the streamwise direction. The augmentation of the average Nusselt number and friction factor resulting from buoyancy was prominent at the entrance region of the pipe, but gradually became weaker further downstream.

Key words: Turbulent flow; Mixed convection; Curved pipe; Entrance region

Nomenclature

a radius of the curved pipe [m]
A area [m^2]
$C_{\varepsilon 1}$, $C_{\varepsilon 2}$, C_μ turbulence model constant
D_n Dean number ($= Re\cdot\delta^{1/2}$)
f_θ local friction factor on the circumference of a pipe ($= \tau_w/\frac{1}{2}\rho u_0^2$)
f_m peripherally averaged frictional factor on one cross-section

$$\left(=\frac{1}{2\pi}\int_0^{2\pi} f_\theta \,\mathrm{d}\theta\right)$$

Gr Grashof number

$$\left(=\frac{\rho^2 g\beta d_h^3}{\mu^2}\Delta T\right)$$

k turbulent kinetic energy [m^2 s^{-2}]

Nu_{fd} fully developed average Nusselt number
Nu_m peripherally averaged Nusselt number on a cross section

$$\left(=\frac{1}{2\pi}\int_0^{2\pi} Nu_\theta \,\mathrm{d}\theta\right)$$

Nu_θ local Nusselt number on the circumference of a pipe [$=(q_w d_h/\Gamma_1)/(T_w-T_b)$]
p pressure [N m^{-2}]
Pr molecular Prandtl number
R_c radius of the coil [m]
Re Reynolds number ($= \rho u_0 d_h/\mu$)
T temperature [K]
T_b fluid bulk temperature on one cross section

$$\left(=\frac{1}{u_s A}\int_0^A u_s T \,\mathrm{d}A\right)\text{[K]}$$

T_w wall temperature [K]
u' root-mean-square turbulent velocity fluctuation [m s^{-1}]
u_0 inlet velocity [m s^{-1}]
u_i velocity component in i-direction ($i=1,2,3$) [m s^{-1}]

* Corresponding author: Professor of Mechanical Engineering and Director of the Hemispheric Center for Environmental Technology.

0017–9310/98 $19.00
PII: S0017–9310(98)00100–8

u_s axial velocity [m]
U_s nondimensional axial velocity ($= u_s/u_0$)
x_i cartesian coordinate in i-direction ($i = 1, 2, 3$) [m].

Greek symbols
β thermal expansion coefficients [K^{-1}]
Γ thermal conductivity [W m^{-1} K^{-1}]
δ curvature ratio of curved pipe ($= a/R_c$)
ε dissipation ratio of turbulent kinetic energy [m^2 s^3]
φ axial angle [°]
μ viscosity [kg m^{-1} s^{-1}]
μ_{eff} effective viscosity [mg m^{-1} s^{-1}]
θ orthogonal azimuthal angle [°]
Θ nondimensional temperature [$=(T-T_w)/(T_b-T_w)$]
ρ density of fluid [kg m^{-3}]
α_T, α_k, α_ε inverse effective Prandtl number for energy, k and ε equation, respectively
τ_w wall shear stress [N m^{-2}].

Subscripts
0 inlet conditions
b bulk quantity
fd fully developed situation
i, j, k, general spatial indices
l, mol laminar or molecular quantity
eff turbulent effective parameters
t turbulent quantity
w wall.

1. Introduction

Turbulent heat transfer to fluids flowing in curved pipes has attracted much attention because of its impact on compact heat exchangers, food and chemical process equipment, and many other processes. Berger et al. [1] and Shah and Joshi [2] have reviewed many experimental, theoretical, and numerical studies on turbulent heat transfer in curved pipes; most of them were limited to fully developed flow. Earlier experimental studies were carried out by Woschni [3], Seban and Mclaughlin [4], and Rogers and Mayhew [5]. Mori and Nakayama [6] and Hogg [7] theoretically calculated the velocity and temperature profile for air flow. Their results also showed good agreement with the numerical predictions conducted by Patankar et al. [8]. Schmidt [9] and Gnielinski [10] established widely used correlation equations of Nusselt number for fully developed turbulent flow in curved pipes. Limited studies on turbulent developing flow in the entrance region of curved pipe are found in literature. For example, Hogg [7] deduced from his test data that the flow becomes fully developed within the first half turn of the coil, and probably even sooner, but no detailed data in the developing turbulent flow were given. Short curved-tube hydrodynamic entrance lengths for turbulent flow were also found by Rower [11].

None of the studies mentioned have been concerned with the effect of buoyancy. Yet, it is well known that both buoyancy and centrifugal forces produce secondary flow. Several studies investigated the effect of buoyancy on laminar convection in curved pipes. Of these researchers, Sillekens [12] successfully carried out the numerical and experimental studies on the mixed laminar convective heat transfer in curved pipes. However, few studies have considered the effect of natural convection on turbulent convective heat transfer in helical pipes, especially on developing turbulent heat transfer in the entrance section of a curved pipe.

This study investigates the mixed turbulent convection heat transfer in the entrance region of curved pipe with uniform wall temperature. The renormalization group (RNG) turbulence model was used to simulate the mixed turbulent flow and heat transfer. The control-volume finite element method (CVFEM) with second-order accuracy, presented by Baliga and Patankar [14], was used to solve the fully elliptic governing equation. The FLUENT/UNS code was used as the numerical solver for the three-dimensional problem. Our emphasis of analysis is focused on the interactive effect of centrifugal force and buoyancy force on the mixed developing turbulent flow and heat transfer. The physics considered in this paper are characterized by Reynolds number $Re = 5\times10^4$, curvature ratio $\delta = 0.05$, with the Grashof number range of $Gr = 5\times10^8$–10^{10}.

2. Analysis

The configuration of a curved pipe is schematically shown in Fig. 1. In general, the practically used coiled pipe is the so-called helicoidal pipe with finite pitch. Manlapaz et al. [15] have shown that the effect of coil pitch is significant only when the pitch is greater than the coil radius R_c. The influence of the pitch on the flow was not

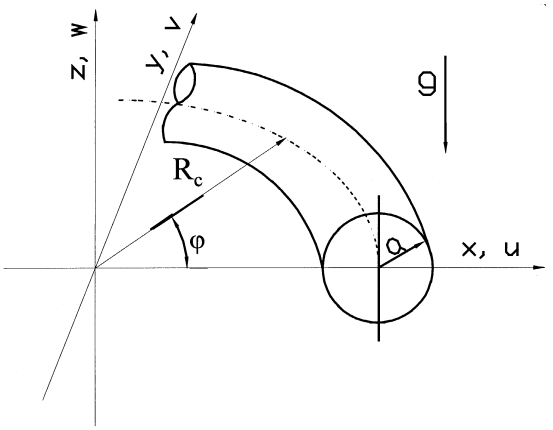

Fig. 1. Schematic of a helical pipe.

addressed in this study, but the conclusion obtained in the present work should be applied for the helical pipes with a lesser pitch. The computation domain is composed of a curved pipe where the axial angle ranges from 0 to 355°. Assuming that the fluid enters the pipe at a constant temperature and at a uniform velocity, u_0, that is sufficiently high to maintain turbulent flow in the curved pipe, the resulting Reynolds number is not less than 2×10^4. The wall is kept at constant temperature, T_w. Thus the turbulent flow and heat transfer develop simultaneously downstream in the curved pipe. To calculate accurately the developing mixed convective heat transfer problem, Aung [16] stated that the fully elliptic governing equations need to be solved. Especially when, in the beginning stage of the mixed turbulent flow in the curved pipe, the secondary flow resulting from the buoyancy force is very strong and the boundary layer is very small, the parabolic formulation is not relevant to the physics of the problem.

The RNG k–ε model proposed by Yakhot and Orszag [17] was chosen to model the turbulent flow and heat transfer in the curved pipe. The major difference between the RNG model and the standard k–ε is that the RNG model was derived using a more rigorous statistical technique. The RNG model provides an analytical formula for turbulent Prandtl number and an analytically derived differential formula for effective viscosity to account for low-Reynolds-number effects, making it more accurate and reliable for a wide class of flow than the standard k–ε model. Also, the RNG model has an additional term in its ε equation that significantly improves the accuracy for rapidly strained flows, such as the turbulent flow in curved pipes.

The RNG k–ε model has the same form as the standard k–ε model. In the cartesian coordinate system, the time-average, fully elliptic differential-governing equations of the turbulent-mixed convection in curved pipe, with inclusion of the buoyancy effect via the Boussinesq approximation, are written in tensor form in the following equations.

Mass

$$\frac{\partial u_i}{\partial x_i}=0 \tag{1}$$

Momentum

$$\frac{\partial}{\partial x_j}(\rho u_i u_j)=\frac{\partial}{\partial x_j}\left[\mu_{\text{eff}}\left(\frac{\partial u_i}{\partial x_j}+\frac{\partial u_j}{\partial x_i}\right)-\frac{2}{3}\mu_{\text{eff}}\frac{\partial u_k}{\partial x_k}\right]-\frac{\partial p}{\partial x_i}-\rho_0 g_i\beta(T-T_0) \tag{2}$$

Energy

$$\frac{\partial}{\partial x_i}(\rho u_i c_p T)=\frac{\partial}{\partial x_i}\left[\alpha_T\left(\mu_{\text{eff}}\frac{\partial T}{\partial x_i}\right)\right]+\frac{\partial u_i}{\partial x_j}\left[\mu_{\text{eff}}\left(\frac{\partial u_i}{\partial x_j}+\frac{\partial u_j}{\partial x_i}\right)-\frac{2}{3}\frac{\partial u_k}{\partial x_k}\right] \tag{3}$$

Turbulent kinetic energy

$$\frac{\partial}{\partial x_i}(\rho u_i k)=\frac{\partial}{\partial x_i}\left[\left(\alpha_k\mu_{\text{eff}}\frac{\partial k}{\partial x_i}\right)\right]+\mu_i S^2+G_b-\rho\varepsilon \tag{4}$$

Dissipation rate of turbulent kinetic energy

$$\frac{\partial}{\partial x_i}(\rho u_i \varepsilon)=\frac{\partial}{\partial x_i}\left[\left(\alpha_\varepsilon\mu_{\text{eff}}\frac{\partial \varepsilon}{\partial x_i}\right)\right]+C_{1\varepsilon}\frac{\varepsilon}{k}\mu_t S^2-C_{2\varepsilon}\rho\frac{\varepsilon^2}{k}-R \tag{5}$$

The effective viscosity, μ_{eff} is calculated by the equation

$$\mu_{\text{eff}}=\mu_{\text{mol}}\left[1+\sqrt{\frac{C_\mu}{\mu_{\text{mol}}}}\frac{k}{\sqrt{\varepsilon}}\right]^2 \tag{6}$$

where μ_{mol} is the molecular viscosity. Equation (6) shows the RNG k–ε model yields an accurate description of how the effective turbulent transport varies with the effective Reynolds number (or eddy scale), allowing accurate extension of the model to low-Reynolds-number and near-wall flows. The coefficients α_T, α_k and α_ε in eqns (3)–(5) are the inverse effect Prandtl number for T, k and ε, respectively. They are computed using the following formula:

$$\left|\frac{\alpha-1.3929}{\alpha_0-1.3929}\right|^{0.6321}\left|\frac{\alpha+2.3929}{\alpha_0+2.3929}\right|^{0.3679}=\frac{\mu_{\text{mol}}}{\mu_{\text{eff}}} \tag{7}$$

where α_0 is equal to $1/Pr$, 1.0, and 1.0, for the computation of α_T, α_k, and α_ε, respectively. S in eqns (4) and (5) is the modulus of the mean rate-of-strain tensor, S_{ij}, which is defined as

$$S=\sqrt{2S_{ij}S_{ij}} \tag{8}$$

where

$$S_{ij}=\frac{1}{2}\left(\frac{\partial u_i}{\partial x_j}+\frac{\partial u_j}{\partial x_i}\right).$$

R in eqn (5) is given by

$$R=\frac{C_\mu\rho\eta^3(1-\eta/\eta_0)}{1+\zeta\eta^3}\cdot\frac{\varepsilon^2}{k} \tag{9}$$

where $\eta=S\cdot k/\varepsilon$, $\eta_0\approx4.38$, $\zeta=0.012$. The model constants C_μ, $C_{1\varepsilon}$, and $C_{2\varepsilon}$ are equal to 0.085, 1.42 and 1.68, respectively. In the RNG k–ε model, the effects of buoyancy on turbulence can be accounted for through G_b in eqn (4). G_b is defined as

$$G_b=\beta g_i\alpha_T\mu_t\frac{\partial T}{\partial x_i} \tag{10}$$

where α_T is the inverse turbulent Prandtl number for energy as defined in eqn (7).

In the near wall zone, the two-layer-based, non-equilibrium wall function is employed for the near-wall treatment flow in curved pipes. This method requires some consideration of mesh, i.e. the cell adjacent to the wall should be located to ensure that the parameter y^+ ($\equiv ru_\tau y/\mu$) or

$$y^*\left(\equiv\frac{\rho C_\mu^{1/4}k_p^{1/2}y_p}{\mu}\right)$$

falls into the 30–60 range. In the present study, the y^+ is adapted into the 35–55 range.

The nonslip boundary condition is imposed on the pipe wall. At the inlet, all dependent variables are assumed to enter the pipe with uniform profile in the direction normal to the inlet plane, i.e.

$$u=u_0, T=T_0, k=k_0, \varepsilon=\varepsilon_0 \tag{11}$$

The inlet boundary values of k and ε are computed from an estimated turbulence intensity, I, and turbulent length scale, l, as follows:

$$k_0=\frac{2}{3}(u_0 I)^2, \varepsilon_0=C_\mu^{3/4}\frac{\kappa_0^{3/2}}{l}$$

The turbulent intensity I, defined as u'/u, is equal to 5%, and the length scale l is set to be $0.07\cdot a$ in the present study. How the computed results are sensitive to the variations of the inlet k and ε was not addressed here.

The setting of the exit boundary condition is an important factor for validation of the solution. As known from Hogg [7] and Rower [11], the forced turbulent flow in curved pipe becomes fully developed within the first turn of the coil or even sooner. In the present study of mixed turbulent flow in the curved pipe, in the situation where the exit boundary condition is unknown, the exit boundary condition is treated as an outflow condition, which means that the diffusion flux for all dependent variables are set to zero at the exit (i.e. a fully developed flow assumed) and an overall mass balance is obeyed. This outflow boundary condition is true if the flow becomes fully developed at a position far upstream from the exit because the accuracy of the exit boundary condition should not affect the flow and heat transfer fields far upstream from the exit. The results computed afterward indicate the mixed turbulent flow and heat transfer become almost fully developed at the axial angle of around 180°. This proves the outflow boundary condition is reasonable.

To represent the results and characterize the mixed-turbulent convection in curved pipes, the following dimensionless variables and parameters are introduced

$$Re=\frac{\rho u_0 d_h}{\mu}, \delta=\frac{a}{R_c},$$

$$D_n=Re\cdot\delta^{1/2}, Gr=\frac{\rho^2 g\beta d_h^3}{\mu^2}\Delta T$$

$$Pr=\frac{\nu}{\alpha}, U_s=\frac{u_s}{u_0}, \quad f_\theta=\frac{\tau_w}{\frac{1}{2}\rho u_0^2}, \quad f_m=\frac{1}{2\pi}\int_0^{2\pi} f_\theta\,d\theta$$

$$T_b=\frac{\int_0^A u_s T\,dA}{\int_0^A u_s\,dA}, \Theta=\frac{T-T_w}{T_b-T_w},$$

$$Nu_\theta=\frac{q_w\cdot d_h}{\Gamma(T_w-T_b)}, Nu_m=\frac{1}{2\pi}\int_0^{2\pi} Nu_\theta\,d\theta \tag{12}$$

where ΔT is the temperature difference between fluid at inflow and the pipe wall, $\Delta T=T_w-T_0$; d_h represents the hydraulic diameter ($2a$) of the pipe; the wall shear stress, τ_w, is computed with the normal velocity gradient at the wall, and the heat flux, q_w, is computed using Fourier's law applied at the wall.

The factors affecting the mixed turbulent flow and heat transfer are sophisticated. It is hard to take account of all factors. But we know the flow and heat transfer characteristics in curved pipe are mainly determined by the secondary flow. According to Sillekens [12], the relative magnitude of the buoyancy driven secondary flow to the centrifugal force driven secondary flow is of order of $\sqrt{Gr}/D_n\sqrt{1+Pr}$. In the present work, we concentrate on analyzing the interactive effect of the centrifugal force and buoyancy force on the mixed turbulent flow and heat transfer.

3. Numerical computation

The governing equations for the turbulent-mixed convective heat transfer in the curved pipe are solved in the Cartesian master coordinate system with a CVFEM similar to that introduced by Baliga and Patankar [14]. A multiblock structured nonuniform grid system, shown in Fig. 2, has been used to discretize the computation domain. Five blocks were fixed into the entire pipe, forming a typical three-dimensional grid system consisting of definite hexahedral elements.

The bounded second-order upwind scheme proposed by Rhie and Chow [18] was employed for the discretization of the convection term in the governing equations, while the diffusion term was computed by means of multi-linear interpolating polynomials. The SIMPLEC algorithm introduced by Van Doormaal and Raithby [19] was employed to resolve the coupling between velocity and pressure. Because of the intensive nonlinearity and coupling features of this problem, the under-

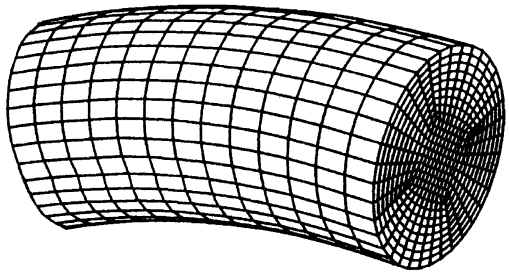

Fig. 2. Unstructured grid of the helical pipe.

relaxation technique was applied to the iteration process to accelerate convergence. The convergence criterion of

$$\frac{R_{\Phi}^{n}}{R_{\Phi}^{m}} \leqslant 10^{-4} \tag{13}$$

was applied for all equations, where R_{Φ}^{m} refers to the maximum residual value summed over all the computation cells after mth (usually $m = 5$) iteration, and R_{Φ}^{n} the value at nth iteration. To test the criterion independence, another convergence criterion of 10^{-5} is applied to a case. The difference of computed peripherally averaged Nu numbers of the two convergence criterion is within 1%.

The grid independence was investigated in the analysis by adopting different grid distributions. Table 1 is a comparison of the predicted results at the outlet with different grid distributions (section × axial). The sectional number refers to the total number of elements on the cross section normal to the axial direction of the pipe. Table 1 shows that the grid system of 500×160 adequately ensures a satisfactory solution. Thus the present computations are based on the grid system of 500×160. On a Sun Sparc20 workstation, approximately 350–400 iterations were needed to obtain the converged solution.

4. Results and discussion

The numerical simulations in the present study are based on the constant physical properties for water ($Pr = 5$). To examine the accuracy of numerical computation, the predicted results were compared with experimental results. Due to the limited data on developing turbulent mixed heat transfer in curved pipes, the present predictions were compared mainly with previous experimental results on fully developed forced convective heat transfer. Relevant to this comparison is that in turbulent convective heat transfer, temperature profiles and Nusselt numbers are independent of the thermal boundary condition for $Pr \geqslant 0.7$, according to data from Shah and Joshi [2].

Table 1
Grid independence test

Elements (sectional × axial)	f_m	$(T_b - T_0)/(T_w - T_0)$	Nu_m
245×100	0.005424	0.276	328.6
320×120	0.005763	0.278	331.3
500×120	0.005875	0.286	336.7
720×120	0.005989	0.285	336.8
500×160	0.006112	0.283	337.5
500×200	0.006110	0.283	337.4

$Re = 5 \times 10^4$, $\delta = 0.05$, $Gr = 0$

Tables 2 and 3 show the comparisons of the predicted results with the previous experimental and theoretical results. The typical case for the comparison is for water at $Re = 5 \times 10^4$, $\delta = 0.05$, $Gr = 0$. For this case, the flow and heat transfer can be thought to be fully developed at the outlet of one turn coil of the curved pipe. The computed fully developed friction factor is equal to 0.006112, which is a little underpredicted in contrast with experimental results. The computed, fully developed Nusselt number for this case is equal to 337.8, which shows good agreement with the experimental results and indicates that the turbulence model and the computation code employed are sufficiently accurate to model the mixed turbulent heat transfer in the entrance region of the curved pipe.

4.1. Development of flow and temperature fields

It is well known that the characteristics of convective heat transfer in curved pipes are strongly dependent on the behavior of the secondary flow. As stated above, in mixed turbulent convection in the curved pipes, the secondary flow patterns are caused by both centrifugal and buoyancy force. The relative magnitude of the buoyancy-driven secondary flow to the centrifugal-force-driven secondary flow is of the order of $\sqrt{Gr}/D_n\sqrt{1+Pr}$. In this study, interest is focused on the conditions of $Re = 5 \times 10^4$, $\delta = 0.05$, $Pr = 5$ with six different Grashof number of $Gr = 0$, 5×10^8, 10^9, 2×10^9, 5×10^9 and 10^{10}, corresponding to different $\sqrt{Gr}/D_n\sqrt{1+Pr}$ ratios of 0, 0.8165, 1.155, 1.633, 2.582 and 3.65, respectively. The development of the secondary flow pattern visualized by vectors is shown in Fig. 3. The axial velocity distribution visualized by contours of equal velocity is shown in Fig. 4. The secondary velocity vectors and the dimensionless isotachs on the cross-sectional plane at different axial positions are drawn for three cases: $Gr = 0$, 10^9, and 10^{10}, respectively. In Fig. 3, the scaling of the secondary flow produces a vector length equal to the diameter of the pipe, which corresponds to 1.35 times average axial velocity. In Fig. 5 the difference in velocity magnitude between different dimensionless isotachs equals 0.03.

Figure 3(I) shows the situation in which only centrifugal force exists. At $\varphi = 15^\circ$, the secondary flow is weak. Due to the effect of centrifugal force, the flow in the core of the pipe begins to be forced to the outer bend. At $\varphi = 45^\circ$, two symmetric secondary vortices emerge, and the secondary flow through the core region seems to increase to the maximum. As a result, the maximum axial velocity is shifted towards the outer bend, shown in Fig. 4. In the meantime, the magnitude of maximum velocity increases with the development of the boundary layer. Further downstream, the secondary flow through the core region decreases because of the outward shift of the main flow. After the position of $\varphi = 180^\circ$, the dimen-

Table 2
Comparison of fully developed friction factor with previous experimental results

Previous studies	Experiments or theoretical correlations	Deviation from presented elliptic numerical study (%)
Ito [23]	$f_{fd}\left(\frac{R_c}{a}\right)^{0.5} = 0.00725 + 0.076\left[Re\left(\frac{R_c}{a}\right)^{-2}\right]^{-0.25}$	8.83
Seban and Mclaughlin [4]	$\frac{f_{fd}}{f_s} = \left[Re\cdot\left(\frac{a}{R_c}\right)^2\right]^{1/20}, \quad f_s = \frac{1}{4}\cdot\frac{0.3164}{Re^{0.25}}$	9.24

Table 3
Comparison of fully developed Nusselt number with previous experimental results

Previous studies	Experiments or theoretical correlations	Deviation from presented elliptic numerical study (%)
Rogers and Mayhew [5]	$Nu_{fd} = 0.023Re^{0.85}\cdot Pr^{0.4}\cdot\delta^{0.1}$	−5.6
Schmidt [9]	$Nu_{fd}/Nu_s = 1.0 + 3.6[1-(a/R)](a/R)^{0.8}$ $Nu_s = 0.023Re^{0.8}\cdot Pr^{0.4}$	−2.43
Gnielinski [10]	$Nu_{fd} = \frac{(f/8)Re\cdot Pr}{1+12.7\sqrt{f/8}(Pr^{2/3}-1)}\left(\frac{Pr}{Pr_w}\right)^{0.14}$ $f = [0.3164/Re^{0.25} + 0.03\delta^{0.5}](\mu_w/\mu)^{0.27}$	5.27

sionless isotachs for $Gr = 0$ show almost no change, as revealed in Fig. 4(d) and (e) for case I, indicating a fully developed situation at the outlet of the pipe.

Cases II and III show how the velocity fields were affected by an increasing buoyancy force. The buoyancy force results in a secondary flow pattern similar to that caused by centrifugal force, except the orientation is different. However, under the interaction of both buoyancy and centrifugal force, the flow loses symmetry. For $Gr = 10^9$, (case II in Fig. 3), the centrifugal effect and the buoyancy effect seem to be equally important ($\sqrt{Gr}/D_n\sqrt{1+Pr} = 1.155$), that is, the direction of secondary flow in the core region is directed bottom-outwards at about 45°, and the intensity of secondary flow is higher compared with case I. Near the entrance (at $\varphi = 15°$) the buoyancy effect seems to be small for case II. The axial isotachs in Fig. 4(II) show how the medium in the pipe is conveyed by the secondary flow. It is interesting to note that although the secondary flow and isotachs pattern for case II have rotated clockwise, their symmetry seems not to be affected.

For higher Grashof number (case III in Fig. 3 and Fig. 4), the buoyancy effect is dominant over the centrifugal effect even at the beginning of the curved pipe. At $\varphi = 45°$, a complex secondary flow developed, and the symmetry was destroyed. The most remarkable feature of the velocity fields for higher Grashof number was the occurrence of a third vortex near the center of the pipe, which was also found in laminar mixed convection by Sillekens [12] and Cheng and Yuen [20]. The third vortex is driven by shear effects of the upright vortex. From case III in Fig. 4, it can be seen that the axial velocity field is also affected by the third vortex. However, at $\varphi = 180°$, the third vortex disappears, and the intensity of secondary flow decreases. This is because buoyancy force decreases with the fluid medium being further heated. When $\varphi \geqslant 180°$, the flow in the pipe stratifies, and the maximum axial velocity is located towards the bottom of the pipe. Meanwhile, by comparing the dimensionless isotachs contour at $\varphi = 180°$ with those downstream (not listed here due to the length limitation), it was found that the dimensionless velocity distribution almost ceases to change and the same fact was also found in the dimensionless fields, which meant that the flow and heat transfer became almost fully developed at the position of $\varphi = 180°$. Therefore, the assumption of outflow boundary at the exit plane ($\varphi = 355°$) is reasonable.

Figure 5 shows the development of temperature with

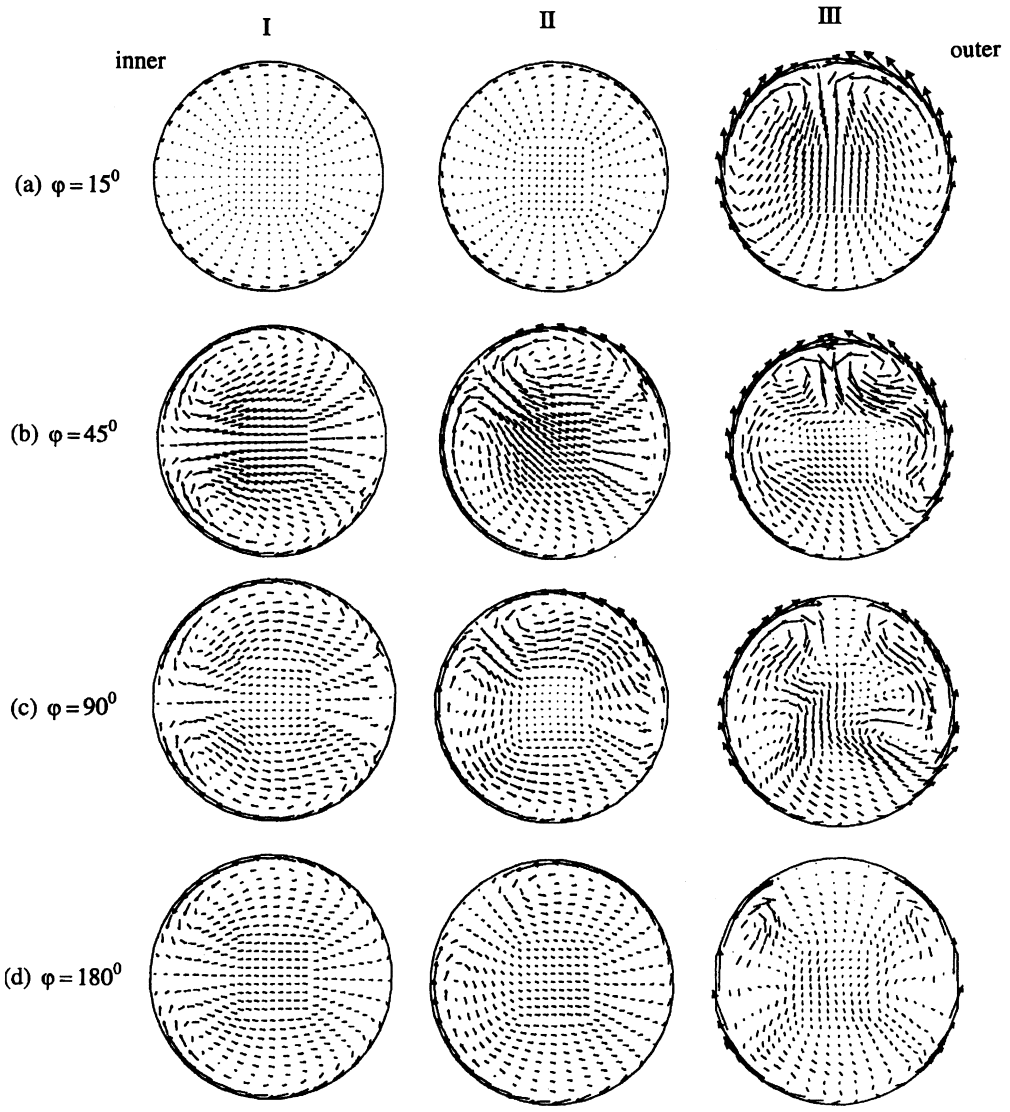

Fig. 3. Computed secondary velocity vectors at different axial positions at $Re = 5 \times 10^4$, $\delta = 0.05$ and $Pr = 5$: (I) $Gr = 0$; (II) $Gr = 10^9$; (III) $Gr = 10^{10}$.

contours of equal dimensionless temperature at different axial positions. The difference between the successive isotherms is 0.03. The development of temperature field is very similar to that of axial velocity field. In Fig. 5, case I represents the situation of pure forced convection without the buoyancy effect. By comparing the dimensionless temperature contour at $\varphi = 180^\circ$, and $\varphi = 350^\circ$, one can see that the temperature distribution almost ceases to change, indicating that the temperature boundary layer has been fully developed. The effect of buoyancy force on the temperature fields is implemented by the secondary flow, while the secondary flow is strongly effected by the temperature fields.

4.2. Development of Nusselt number and friction factor

Figure 6 shows the peripheral distribution of local Nusselt number at different axial positions. The curves marked with different numbers represents the cases with different buoyancy effects. At $\varphi = 15^\circ$, centrifugal and buoyancy effects on the flow have not been established, so the local Nusselt number distribution for all Grashof numbers is almost uniform, except for a slight variation with a higher Grashof number ($Gr = 10^{10}$), which seems to indicate that the buoyancy effect occurs somewhat sooner at higher Grashof numbers. From the axial position at $\varphi = 30^\circ$, both the centrifugal and buoyancy force

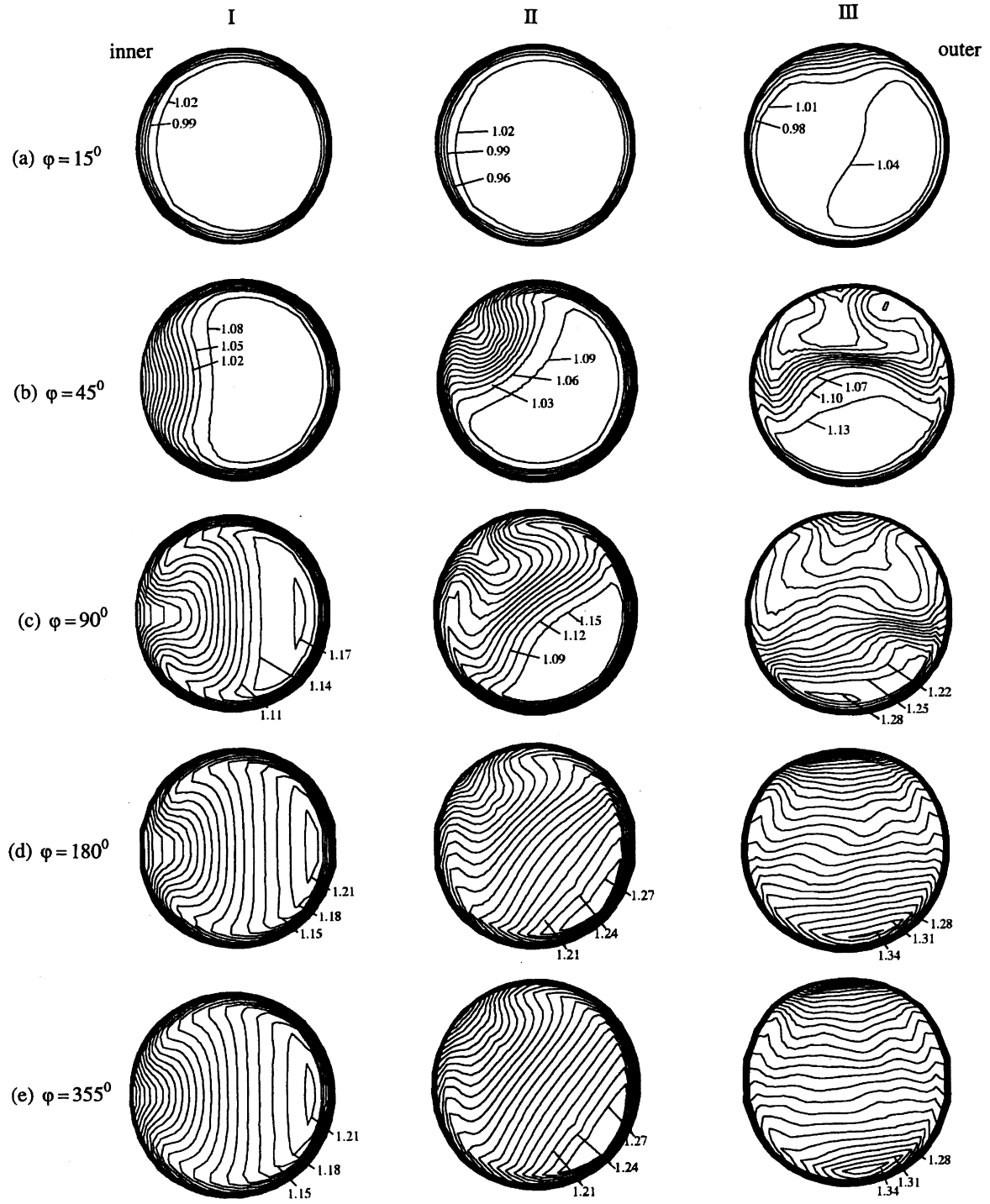

Fig. 4. Computed dimensionless isotachs at different axial positions at $Re = 5 \times 10^4$, $\delta = 0.05$ and $Pr = 5$; (I) $Gr = 0$; (II) $Gr = 10^9$; (III) $Gr = 10^{10}$.

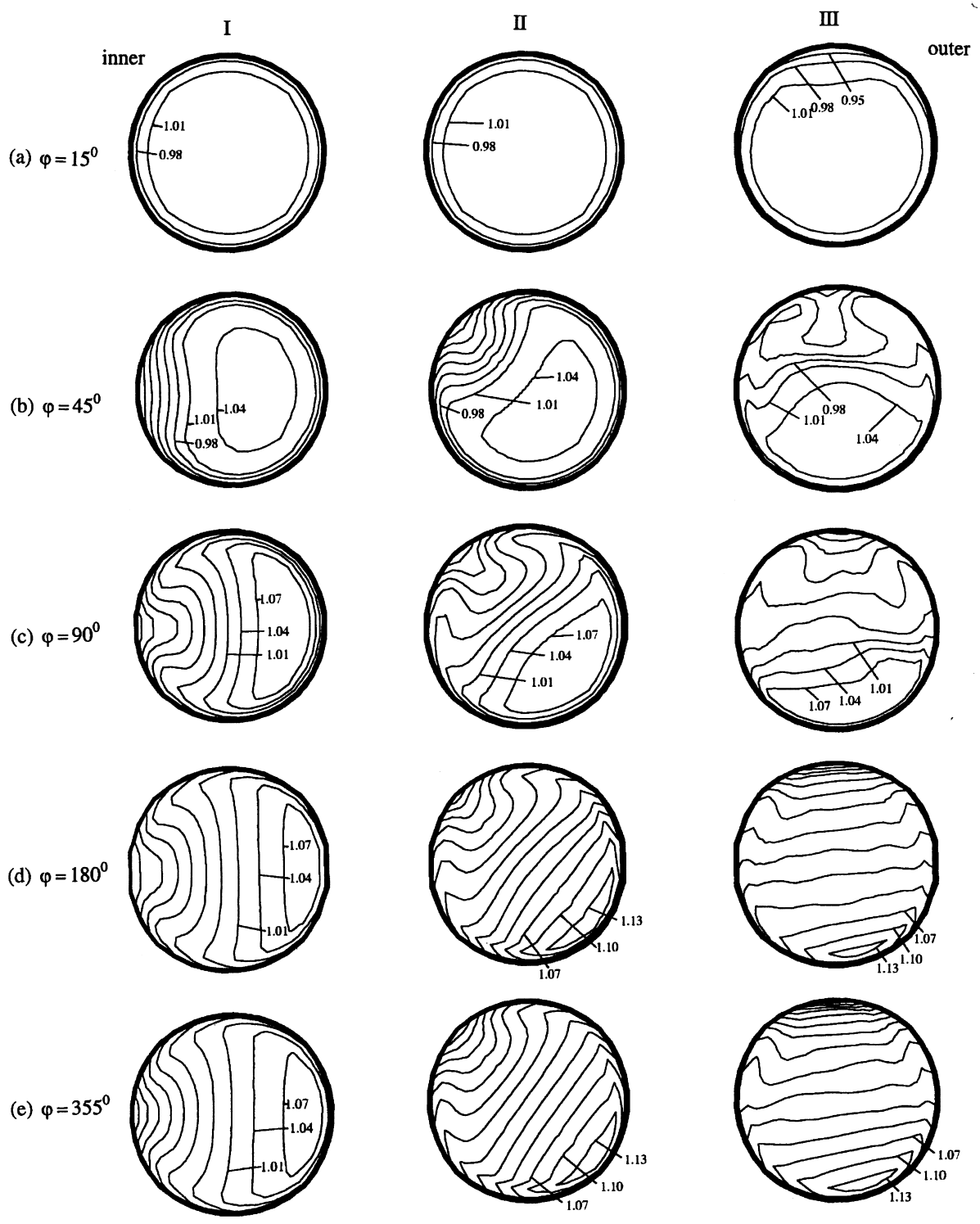

Fig. 5. Computed dimensionless isotherms at different axial positions at $Re = 5 \times 10^4$, $\delta = 0.05$ and $Pr = 5$: (I) $Gr = 0$; (II) $Gr = 10^9$; (III) $Gr = 10^{10}$.

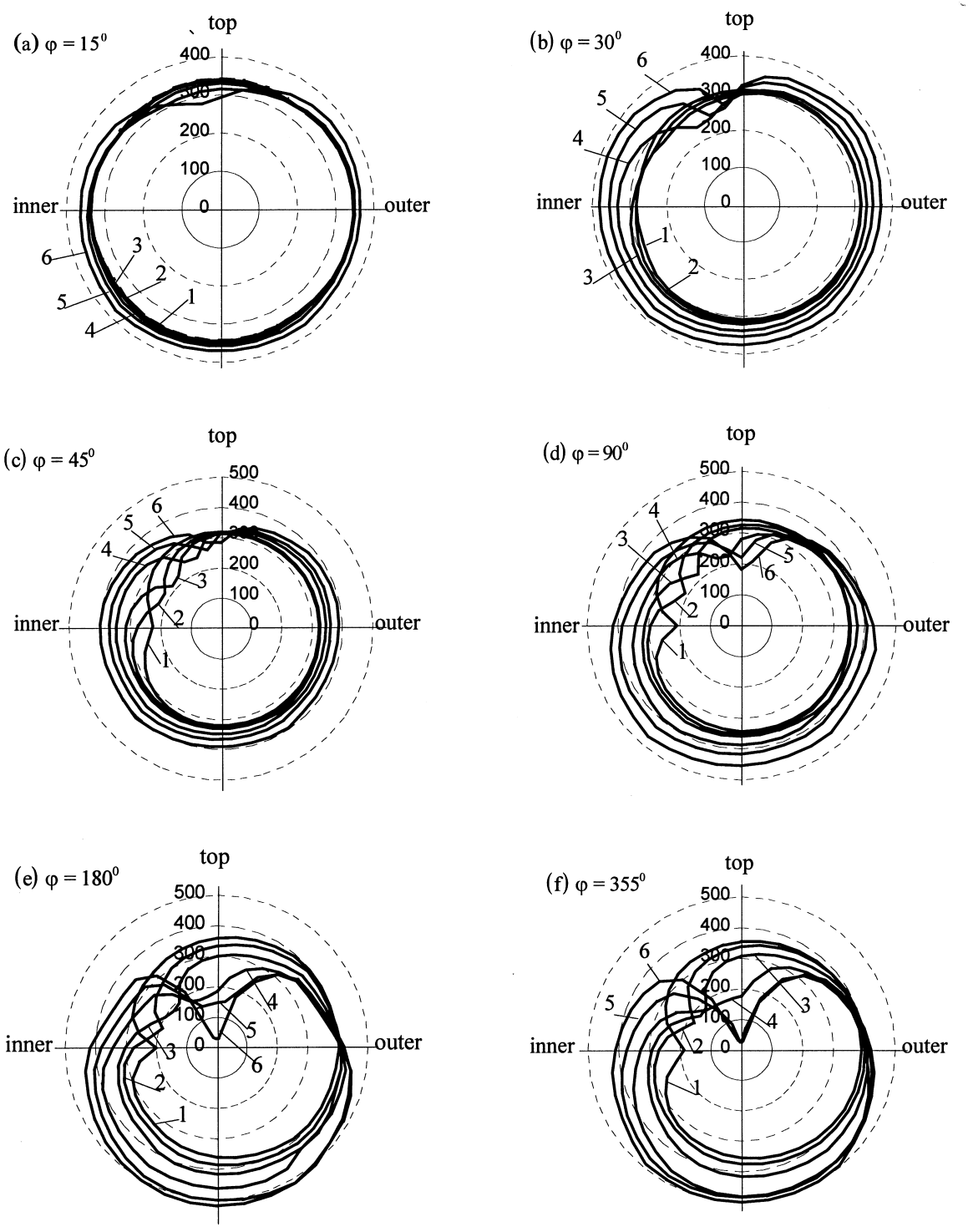

Fig. 6. Distribution of the peripherally local Nusselt number at $Re = 5\times10^4$, $\delta = 0.05$ and $Pr = 5$. (1) $Gr = 0$; (2) $Gr = 5\times10^8$; (3) $Gr = 10^9$; (4) $Gr = 2\times10^9$; (5) $Gr = 5\times10^9$; (6) $Gr = 10^{10}$.

give rise to larger effect on the secondary flow and temperature boundary layer, resulting in obvious peripheral variation of the local Nusselt number. On the other hand, it was noted that the peripheral distribution pattern of the local Nusselt number rotates clockwise as the Gr number increases. This phenomenon was also found in numerical studies on mixed laminar convection in curved pipes by Futagami and Aoyama [21] and Lee et al. [22], and in experimental research on mixed convective heat transfer by Xin and Ebadian [13]. Generally, in the situation in which only centrifugal force is active, the medium in the core region of the curved pipe is forced toward the outer wall, resulting in a maximum Nusselt number at the outer wall and a minimum one on the inner wall. Curve 1 in Fig. 6 shows this. However, due to the interaction of centrifugal and buoyancy forces, the minimum Nusselt number shifts upwards from the inner bend, and the maximum shifts downwards from outer bend. Figure 6 reveals that the higher the Grashof number, the more significant the Nusselt number distribution clockwise rotation, and, at the same time, the larger the deviation of the maximum and minimum Nusselt number. For example, at $\varphi = 180^\circ$ with a higher Grashof number ($Gr = 10^{10}$), the minimum Nusselt number shifts upward to the top of the pipe and the maximum shifts downward to the bottom of the pipe, indicating the buoyancy effect is dominant to the secondary flow, and the ratio of the maximum to the minimum Nusselt number is 12.5. While in the case of pure forced convection ($Gr = 0$) the ratio is about 1.5.

The peripherally averaged Nusselt number in the curved pipe is shown in Fig. 7. Curve 1 is when $Gr = 0$, and curve 2–6 are when $Gr = 5\times10^8$, 10^9, 2×10^9, 5×10^9, and 10^{10}, respectively. The curves for all situations show initial decreases of the Nusselt number. Initially, the secondary flow gives rise to little influence on the temperature boundary layer at the wall [as shown in Fig. 5(a)]. After reaching a minimum, the average Nusselt number begins to increase with the axial position. This is a sign that the secondary flow resulting from the centrifugal and buoyancy force starts to influence the temperature boundary layer. For variations in the Grashof number, the position at which the average Nusselt number reaches the minimum and begins to increase is different. It has been observed that the higher the Grashof number, the sooner the peripherally averaged Nusselt number reaches the minimum. Further downstream, the Nusselt number increases gradually and reaches a maximum, indicating the effect of the secondary flow on the temperature boundary layer reaches the maximum. Meanwhile, at higher Grashof numbers this local maximum occurs sooner. After the increasing stage, the peripherally averaged Nusselt number then decreases with the increase of axial position. Clearly the peripherally averaged Nusselt numbers for all Grashof numbers show oscillation, especially in the stage after the maximum. The similar oscillatory behavior of the Nusselt number was also found in previous numerical studies by Patankar [23] and Sillekens [12]. The reason for the oscillation behavior lies in the circulating secondary flow. Moreover, the buoyancy force generally enhances heat transfer. At the entrance region of the pipe, the augmentation of the peripherally averaged Nusselt number resulting from buoyancy is relatively prominent, but gradually becomes weaker further downstream with the development of boundary layer. However, if $Gr \leqslant 10^9$, or $\sqrt{Gr}/D_n\sqrt{1+Pr} \leqslant 1.155$, the effect of buoyancy force on the peripherally averaged Nusselt number is very slight within the whole regional, though the buoyancy shifts the maximum and the minimum local Nusselt numbers, as Fig. 6 indicates. This qualitatively agrees with the conclusion made by Xin and Ebadian [13].

The development of the friction factor, shown in Fig. 8 is quite similar to the development of the peripherally

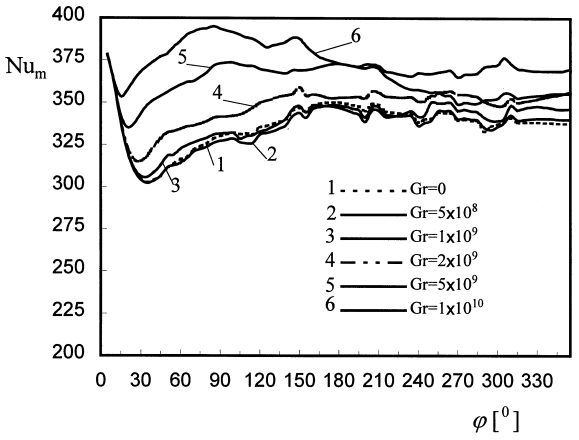

Fig. 7. Development of the peripherally averaged Nusselt number with axial position.

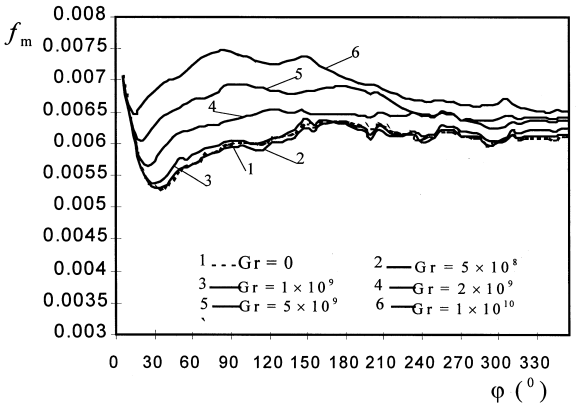

Fig. 8. The development of peripherally averaged friction factor with axial position.

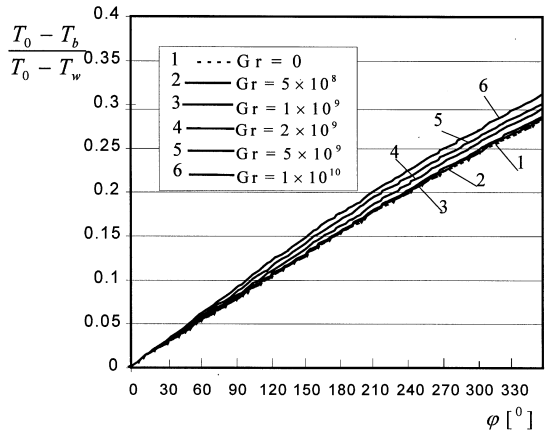

Fig. 9. The development of the dimensionless bulk temperatures with axial position.

averaged Nusselt numbers shown in Fig. 7. Figure 8 shows that the friction rises due to the effects of buoyancy force. For the cases of $Gr \geqslant 5 \times 10^9$, the local maximum of the peripherally averaged friction factor is observed around the position of $\varphi = 90^\circ$. When $Gr \leqslant 10^9$, the effect of buoyancy force on the peripherally averaged friction factor is also very slight within the whole region.

The ratio of the energy gained by fluid to the most possibly theoretical value can be represented by the dimensionless bulk temperature, defined as $(T_0 - T_b)/(T_0 - T_w)$. The development of the dimensionless bulk temperature with axial position is given in Fig. 9. Figure 9 shows that the bulk temperature of the fluid increases almost linearly with the axial position in the entrance region of the curved pipe, but locally shows slight wavy behavior because of the oscillatory development of the peripherally averaged Nusselt number. At the outlet of the pipe, the fluid has gained about 30% of its energy, but the temperature difference between different Grashof numbers is small, which indicates that the effect of buoyancy on the total heat transfer efficiency is insignificant. This is because the buoyancy force effect increases the peripherally averaged Nusselt number only within a little short length in the beginning part of the curved pipe though it alters greatly the local Nusselt number distribution.

5. Conclusion

Three-dimensional turbulent mixed convective heat transfer in the entrance region of curved pipe has been studied numerically with a CVFEM. The fully elliptic approach is used for the numerical computation. The computed results of fully developed heat transfer show good agreement with existing experimental data.

The numerical computations reveal the development of flow and temperature fields. The buoyancy force changes the orientation of the secondary flow and the distribution of axial velocity and temperature. At higher Grashof numbers, the flow shows the existence of three vortices. Those vortices are attributed to an effective heat transfer augmentation mechanism.

The local Nusselt number is affected significantly by buoyancy force. The buoyancy force causes the secondary flow pattern and the peripheral distribution of local Nusselt number to rotate clockwise, and the deviation between the maximum and minimum Nusselt number increases greatly with the increase of the Grashof number.

The peripherally averaged Nusselt number and friction factor exhibit an oscillatory behavior in the entrance region of the curved pipe. The buoyancy effect increases generally the magnitude of the peripherally averaged Nusselt number within the beginning part of the pipe only when $\sqrt{Gr}/D_n\sqrt{1+Pr} \geqslant 1.2$.

Acknowledgement

The authors gratefully acknowledge the financial support of the National Science Foundation (NFS) under Grant No. CTS-9017732.

References

[1] Berger SA, Talbot L, Yao, SL. Flow in curved pipes. Annual Review of Fluid Mechanics 1983;15:461–512.
[2] Shah RK, Joshi SD. Convective heat transfer in curved ducts. In : Kakac S, Shah RK, editors. Handbook of single-phase convective heat transfer. New York : John Wiley and Sons, 1987.
[3] Woschni G. Untersuchung des warmeubergangs und des druckverlusts in gekrummten rohren. Dr.-Ing. Diss. TH Dresden, DDR, 1959.
[4] Seban RA, McLaughlin EF. Heat transfer in tube coils with laminar and turbulent flow. Int J Heat Mass Transfer 1963;6:387–95.
[5] Rogers GFC, Mayhew YR. Heat transfer and pressure loss in helical coiled tubes with turbulent flow. Int J Heat Mass Transfer 1964;7:1207–16.
[6] Mori Y, Nakayama W. Study on forced convective heat transfer in curved pipes (2nd report, turbulent region). Int J Heat Mass Transfer 1967;10:37–59.
[7] Hogg GW. The effect of secondary flow on point heat transfer coefficients for turbulent flow inside curved tubes. Ph.D. Thesis, University of Idaho, 1968.
[8] Patankar SV, Pratap VS, Spalding DB. Prediction of turbulent flow in curved pipes. J Fluid Mech 1975;57:583–95.
[9] Schmidt EF. Warmeubergang und druckverlust in Rohrschlangen. Chemie-Ing-Techn. 1967;36:781–9.
[10] Gnielinski V. Heat transfer and pressure drop in helically coiled tubes. Proceedings of the 8th International Heat

Transfer Conference, Vol. 6. Washington, DC: Tayler and Francis, 1986, p. 2847–54.
[11] Rowe M. Measurements and computations of flow in pipe bends. J Fluid Mech 1970;43:771–83.
[12] Sillekens JJM. Laminar mixed convection in ducts. Ph.D. Thesis, Technische Universiteit Eindhoven, 1995.
[13] Xin RC, Ebadian MA. Influence of buoyance on convective heat transfer in helicoidal pipes. Journal of Thermophysics and Heat Transfer 1997;11:196–202.
[14] Baliga BR, Patankar SV. A control volume finite-element method for two-dimensional fluid and heat transfer. Numerical Heat Transfer 1983;6:245–61.
[15] Manlapaz RL, Churchill SW. Fully developed laminar flow in a helically coiled tube of finite pitch. Chem Eng Commun 1980;7:57–78.
[16] Aung W. Mixed convection in internal flows. In: Kakac S, Shah R, Aung W, editors. Handbook of single-phase convective heat transfer. John Wiley and Sons, 1987.
[17] Yakhot V, Orszag SA. Renormalization group analysis of turbulence: I. basic theory. J Scientific Computing 1986;1(1):1–51.
[18] Rhie CM, Chow WL. Numerical study of the turbulent flow past an airfoil with trailing edge separation. AIAA Journal 1983;21(11):1525–32.
[19] Van Doormaal JP, Raithby GD. Enhancements of the SIMPLE method for predicting incompressible flow problem. Numerical Heat Transfer 1984;7:147–58.
[20] Cheng KC, Yuen FP. Flow visualization experiments on secondary flow patterns in an isothermally heated curved pipe. Journal of Heat Transfer 1987;109:55–61.
[21] Futagami K, Aoyama Y. Laminar heat transfer in a helically coiled tube. Int J Heat Mass Transfer 1988;31:387–96.
[22] Lee JB, Simon HA, Chow JCF. Buoyancy in developed laminar curved tubes flow. Int J Heat Mass Transfer 1985;28:631–40.
[23] Ito H. Friction factors for turbulent flow in curved pipes. Journal of Basic Engineering. Transaction of ASME 1959;81:123–4.